NASA/TP—2000–210075

Laser Transmission Measurements of Soot Extinction Coefficients in the Exhaust Plume of the X–34 60k-lb Thrust Fastrac Rocket Engine

C.C. Dobson, R.H. Eskridge, and M.H. Lee
Marshall Space Flight Center, Marshall Space Flight Center, Alabama

March 2000

The NASA STI Program Office…in Profile

Since its founding, NASA has been dedicated to the advancement of aeronautics and space science. The NASA Scientific and Technical Information (STI) Program Office plays a key part in helping NASA maintain this important role.

The NASA STI Program Office is operated by Langley Research Center, the lead center for NASA's scientific and technical information. The NASA STI Program Office provides access to the NASA STI Database, the largest collection of aeronautical and space science STI in the world. The Program Office is also NASA's institutional mechanism for disseminating the results of its research and development activities. These results are published by NASA in the NASA STI Report Series, which includes the following report types:

- TECHNICAL PUBLICATION. Reports of completed research or a major significant phase of research that present the results of NASA programs and include extensive data or theoretical analysis. Includes compilations of significant scientific and technical data and information deemed to be of continuing reference value. NASA's counterpart of peer-reviewed formal professional papers but has less stringent limitations on manuscript length and extent of graphic presentations.

- TECHNICAL MEMORANDUM. Scientific and technical findings that are preliminary or of specialized interest, e.g., quick release reports, working papers, and bibliographies that contain minimal annotation. Does not contain extensive analysis.

- CONTRACTOR REPORT. Scientific and technical findings by NASA-sponsored contractors and grantees.

- CONFERENCE PUBLICATION. Collected papers from scientific and technical conferences, symposia, seminars, or other meetings sponsored or cosponsored by NASA.

- SPECIAL PUBLICATION. Scientific, technical, or historical information from NASA programs, projects, and mission, often concerned with subjects having substantial public interest.

- TECHNICAL TRANSLATION. English-language translations of foreign scientific and technical material pertinent to NASA's mission.

Specialized services that complement the STI Program Office's diverse offerings include creating custom thesauri, building customized databases, organizing and publishing research results…even providing videos.

For more information about the NASA STI Program Office, see the following:

- Access the NASA STI Program Home Page at ***http://www.sti.nasa.gov***

- E-mail your question via the Internet to help@sti.nasa.gov

- Fax your question to the NASA Access Help Desk at (301) 621–0134

- Telephone the NASA Access Help Desk at (301) 621–0390

- Write to:
  NASA Access Help Desk
  NASA Center for AeroSpace Information
  7121 Standard Drive
  Hanover, MD 21076–1320

NASA/TP—2000–210075

Laser Transmission Measurements of Soot Extinction Coefficients in the Exhaust Plume of the X–34 60k-lb Thrust Fastrac Rocket Engine

C.C. Dobson, R.H. Eskridge, and M.H. Lee
Marshall Space Flight Center, Marshall Space Flight Center, Alabama

National Aeronautics and
Space Administration

Marshall Space Flight Center • MSFC, Alabama 35812

March 2000

TRADEMARKS

Trade names and trademarks are used in this report for identification only. This usage does not constitute an official endorsement, either expressed or implied, by the National Aeronautics and Space Administration.

Available from:

NASA Center for AeroSpace Information
7121 Standard Drive
Hanover, MD 21076–1320
(301) 621–0390

National Technical Information Service
5285 Port Royal Road
Springfield, VA 22161
(703) 487–4650

TABLE OF CONTENTS

1. INTRODUCTION 1

2. THEORY 2

3. EXPERIMENT 5

4. DATA ANALYSIS 8

5. RESULTS AND CONCLUSIONS 12

REFERENCES 25

LIST OF FIGURES

1. Mie theory calculations for lognormal particle distributions. The ratio of the mean volume to the mean cross section gives the scaling of mass density with extinction coefficient (eq. (3)). The key parameters are λ=514.5 nm, m=1.9+i0.6, and FWHM for $p(x)$ is 0.75 $\bar{x}$ 3

2. Schematic for the Fastrac transmissometer 5

3. Photograph of Test Facility 116 Fastrac position showing the 60k-lb engine (right of center) and the laser tranmissometer (left and right flanks) 6

4. Fastrac engine transmissometer beam locations. The four horizontal laser beams, channels 1–4, are perpendicular to the engine axis and lie in a vertical plane ≈1.65 nozzle diameters from the exit plane. The engine axis is tilted ≈6º to the horizontal. Also shown is the position of the FOV for the radiometer used to monitor plume emission 7

5. Radial zones defined for laser transmission through the Fastrac engine plume. The measured radial positions of the laser beams, shown on the lower right in centimeters, are used to define radial zones such that zone boundaries are equidistant from flanking beams. The resulting radial zone boundaries and centers are shown on the upper right, also in centimeters. The laser beams, depicted as gray lines with index k=1–4, are shown on the lower half of the plume, but note that the first beam (channel 1) is actually located above the centerline (see fig. 4) 9

6. Transmission data for short-duration test: test 20. Figure 6(a)–(d) give channels 1–4 normalized to the reference channel and calibrated from the average of signals in pretest and posttest calibration windows, shown as gray regions. Mainstage transmission is also shown in gray 13

7. Transmission data for a long-duration test: test 19. Figure 7(a)–(d) give channels 1–4 normalized to the reference channel and calibrated from the pretest calibration window, shown as a gray region. Mainstage transmission is also shown grayed, and engine startup and shutdown are shown as vertical lines. The decline in signal after ≈70 sec is due to heating of the detectors and not to decreasing transmission 15

LIST OF FIGURES (Continued)

8. Extinction coefficient/soot density distributions for test 19. The coefficient (left) and the density (right) are plotted as functions of the radial position in the plume, where zero is the axis. (a) four-beam/four-zone solution (b) and (c) two (underdetermined) solutions in an eight-zone model. The density values are for carbon soot in the Rayleigh limit 19

9. Extinction coefficient/soot density distributions for test 20. The coefficient (left) and the density (right) are plotted as functions of the radial position in the plume, where zero is the axis. (a) four-beam/four-zone solution (b) and (c) two (underdetermined) solutions in an eight-zone model. The density values are for carbon soot in the Rayleigh limit 20

10. Extinction coefficient/soot density distributions for test 23. The coefficient (left) and the density (right) are plotted as functions of the radial position in the plume, where zero is the axis. (a) four-beam/four-zone solution (b) and (c) two (underdetermined) solutions in an eight-zone model. The density values are for carbon soot in the Rayleigh limit 21

11. Extinction coefficient/soot density distributions for test 24. The coefficient (left) and the density (right) are plotted as functions of the radial position in the plume, where zero is the engine axis. (a) four-beam/four-zone solution (b) and (c) two (underdetermined) solutions in an eight-zone model. The density values are for carbon soot in the Rayleigh limit 22

LIST OF TABLES

1. Averages of pretest and posttest calibration signals, normalized to the reference channel, and the fractional difference δS_k (eq. (6)) between those averages for the two short-duration tests 12

2. Average transmissions T_k and their rms deviations Δ_k for the 60k-lb Fastrac engine 14

3. Extinction coefficients α_j from equation (7) and the T_k, and error bars $\Delta\alpha_j$ from equation (7) and the $T_{k,n}$ from equation (9), both in m^{-1}, for radial zones of the Fastrac engine plume for the four-zone model (algebraic solution). The right column is the mass density of Rayleigh soot and the error bar for η_0 is calculated analogously to $\Delta\alpha_j$ 16

4. Center zone extinction coefficients and mean soot densities for the two-zone model. The outer zone (j=1) coefficients are the same as in table 3 17

5. Extinction coefficients α_j, in m^{-1}, from the fitting using equation (10) for radial zones of the Fastrac engine plume for the four-zone, best-fit model (no α<0). Shown on the right are the merit function μ for the fit, also in m^{-1}, and the mean mass density of Rayleigh soot 17

6. Average extinction coefficients $\overline{\alpha}_j$ and error bars $\Delta\alpha'_j$ from equation (11), in m^{-1}, for radial zones of the Fastrac engine plume for the four-zone, best-fit model (no α<0). Shown on the right are the average merit functions, $\overline{\mu}$, for the fits, also in m^{-1}, and the mean mass density of Rayleigh soot 18

7. Time shifts and rms deviations, in μsec, for correlation between emission signals from the laser channels and emission signals from the radiometer; the FOV of the radiometer is on the engine axis ≈76 cm from the exit plane. Numbers in parentheses are deviations in percentage 23

LIST OF ACRONYMS

ADC	analog-to-digital converter
f/	f-number
FOV	field of view
FWHM	full width at half maximum
lox	liquid oxygen
MSFC	Marshall Space Flight Center
rms	root mean square
Si	silicon

NOMENCLATURE

j	index for plume radial zones
k	index for laser channels
L	path length of the beam through the plume
L_{kj}	path length through zone j of beam k
M	number of zones
N	number of beams
n	number density of soot particles
P	laser power entering one of the integrating spheres
P_0	total output of the laser
S_k	normalized pretest signal
S'_k	normalized posttest signal
T	transmission, the fraction of the laser irradiance transmitted by the plume
T_k	mean transmission of the kth beam
α_j	extinction coefficient in the jth zone
$\overline{\alpha}_j$	average extinction coefficient
Δ_k	deviation of the (measured) transmissions about the mean, T_k
$\Delta\alpha'_j$	error bars for the radial zones of the plume for the four-zone, best-fit model
δS_k	calibration error for the kth laser channel
η	mass density of the soot in the plume gases
μ	merit function
$\overline{\mu}$	average merit function
ρ	bulk density of the soot material
σ_e	extinction cross section
σ_s	scattering cross section
$\overline{\upsilon}$	mean volume per particle
$\upsilon(x)$	volume of an x particle

TECHNICAL PUBLICATION

LASER TRANSMISSION MEASUREMENTS OF SOOT EXTINCTION COEFFICIENTS IN THE EXHAUST PLUME OF THE X–34 60k-lb THRUST FASTRAC ROCKET ENGINE

1. INTRODUCTION

Soot is formed in the combustion of hydrocarbons under conditions routinely found in rocket engines and other combustion systems.[1–3] Soot formation is associated with reduced combustion efficiency and is of concern in environmental pollution.[2,3] It is also largely responsible for the strong thermal emission from such flames.[4] For these reasons, the measurement of soot content in hydrocarbon combustors is of interest, and laser-based measurement techniques, which are attractive because they are nonintrusive, have received much attention.[2–5] These techniques hinge on the measurement of laser light either scattered out of, or transmitted through (or both), the flame, and the general goal is determination of the size distribution and number density of the soot particles. Particular laser soot diagnostics include multiple-beam, multiple-angle and multiple-wavelength static scattering and extinction, diffusion broadening spectroscopy, laser Doppler velocimetry,[3] and dynamic scattering.[5]

This technical memorandum describes soot extinction measurements made using a four-channel laser transmissometer in the exhaust plume of the X–34 60k-lb thrust Fastrac rocket engine, fired at Marshall Space Flight Center's (MSFC) Test Facility 116 in the East Test Area in 1998. The Fastrac engine has been developed at MSFC as the main engine for the X–34 technology demonstrator, an experimental launch vehicle being produced at Orbital Sciences Corporation under contract with NASA. The engine is a liquid oxygen (lox)/kerosene combustor with an ablatable nozzle which uses a gas generator cycle and a single turbopump based on the previously developed Marshall Simplex lox pump.[6]

The transmissometer consists of an argon ion laser housed in a semitrailer beside the test stand and a receiver assembly fixed to the test facility. The output of the laser is split into four beams that are passed through the exhaust plume at separate locations in a plane approximately transverse to the engine axis ≈1.65 nozzle diameters from the exit plane. Each of the four beams is then collected at a separate large-target detector mounted in the receiver housing. The large targets were used in an attempt to maintain reliable signals during the operation of the engine, which was of necessity only a few meters from both the transmitter and the receiver. The hostile conditions of the transmission measurements were the primary obstacle to good accuracy in the data.

The transmission data consistently show very small transparency, typically only a few percent, in the central region of the plume, from the center out to ≈30 cm, and substantial transparency beyond that, out to the plume boundary at ≈50 cm. Also indicated is an annular region of higher transparency at ≈15 cm. The radial zone extinction coefficients derived from the transmission measurements have values from 0.5–8.4 m^{-1}, with error bars estimated at 0.03–1.8 m^{-1}. In the spherical carbon particle model of the soot, then, the spatially averaged mass density in the Rayleigh limit of small particles is 0.65±0.03 $\mu g\ cm^{-3}$.

2. THEORY

The optical quantity which is directly measured by the transmission is the extinction coefficient:

$$\alpha = \ln(1/T)/L \quad , \tag{1}$$

where T is the transmission, the fraction of the laser irradiance transmitted by the plume, and L is the path length of the beam through the plume. This coefficient is related to the soot distribution by

$$\alpha = n\bar{\sigma}_e \quad , \tag{2a}$$

where n is the number density of soot particles and

$$\bar{\sigma}_e = \int \sigma_e(x)p(x)dx \tag{2b}$$

is the mean extinction cross section; here, $p(x)$ is the particle distribution function, defined such that the fraction of particles characterized by values of the parameter x in the range dx centered on x is $p(x)dx$, and $\sigma_e(x)$ is the extinction cross section for x particles. If more than one shape is present, equation (2b) can be summed over the distribution functions for the differing shapes. In the simple case of spherical particles only, x represents the diameter of the particle. In any case, the mass density, η, of the soot in the plume gases is then given by[2,7]

$$\eta = \rho\alpha\frac{\bar{\upsilon}}{\bar{\sigma}_e} \quad , \tag{3a}$$

where ρ is the bulk density of the soot material and $\bar{\upsilon}$ is the mean volume per particle:

$$\bar{\upsilon} = \int \upsilon(x)p(x)dx \quad , \tag{3b}$$

where $\upsilon(x)$ is the volume of an x particle.

The extinction coefficient results presented here are thus general and do not depend on the details of the soot composition. Deriving a mass density from the α-distribution, however, generally requires some knowledge of the distribution function and the optical and bulk properties of the soot. As an important reference case, the mass density is evaluated here for small spherical particles using m=1.9+i0.6 for the optical index of refraction of the hot soot.[1,2] In this case, the absorption, which dominates the extinction, is essentially proportional to the volume of the soot, and the characteristic length $\bar{\upsilon}/\bar{\sigma}_e$ is largely insensitive to the form of $p(x)$ and to the mean diameter $\bar{x}$.[2,5,7] In the Rayleigh limit (x is much less than

(«) λ), $\bar{\upsilon} / \bar{\sigma}_e$ is independent of $p(x)$ and is 0.13 μm. As a numerical example, Mie theory calculations[8] of $\bar{\sigma}_e$ performed here for lognormal distributions with mean diameters from 2–20 nm (λ=514.5 nm) and root mean square (rms) widths from 10–20 percent $\bar{x}$ (i.e., full width at half maximum (FWHM) = 0.23 to 0.44 $\bar{x}$) give variation in $\bar{\upsilon} / \bar{\sigma}_e$ of ≈2 percent. For the small particle carbon soot, then,

$$\eta_0(\mu\text{g cm}^{-3}) \cong 26\ \alpha(\text{cm}^{-1}) \quad , \tag{4}$$

where $\rho = 2$ g cm^{-3} has been used.[2,9] For somewhat larger particles, up to diameters of roughly $\lambda/2$, a value of $\bar{\upsilon} / \bar{\sigma}_e = 0.049$ μm (0.057 for the index used here) has been shown to provide agreement with previous measurements in carbonaceous smokes.[2,7] Mie calculations of $\bar{\upsilon}/\bar{\sigma}_e$ as function of $\bar{x}$ for a 40-percent rms (FWHM=0.75 $\bar{x}$) lognormal distribution are given in figure 1. The curve shows a minimum of ≈0.43 of the Rayleigh value at $\bar{x} = 0.136$ μm and then increases, becoming greater than twice the Rayleigh value near $\bar{x} = 0.75$ μm and thereafter increasing dramatically.

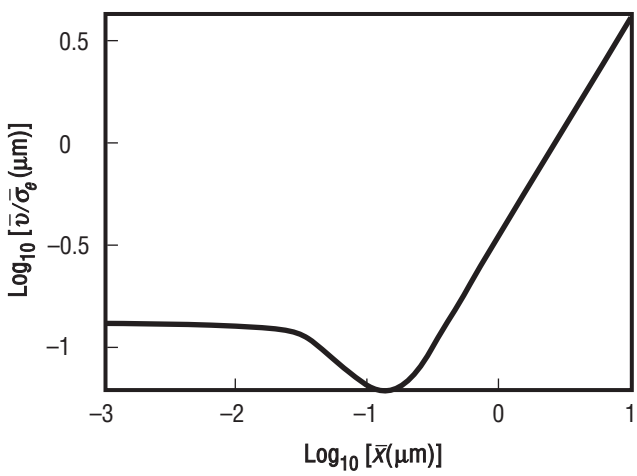

Figure 1. Mie theory calculations for lognormal particle distributions. The ratio of the mean volume to the mean cross section gives the scaling of mass density with extinction coefficient (eq. (3)). The key parameters are λ=514.5 nm, m=1.9+i0.6, and FWHM for $p(x)$ is 0.75 $\bar{x}$.

For the case of aspherical particles, a number of models exist which have been applied in various conditions to compare the scattering and extinction properties of such particles with those of their spherical counterparts; i.e., spherical particles of equal volume (or cross-sectional area).[7] The results indicate that, in the present case, asphericity of the soot particles may be expected generally to increase the cross sections, but not by more than a factor of 2. An interesting point, in this connection, is that for the exemplary, if limited, case of spheroidal particles, the cross sections are appreciably larger than the equal volume spherical cross sections only for the small particles (x<≅200 nm). Thus, the assumption of spherical particles, if faulty, is likely to result in modest overestimates of the actual mass density.

Because of the small collection solid angle in the experiment (half angle = 0.85°), forward-scattering corrections[2] to the transmissions here are negligible: $\int_{\Delta\Omega} \sigma_s(x,\Omega)\, d\Omega < 1.5\times10^{-5}\sigma_e(x)$, all x (and very much less for small particles). It is also expected, because of this small collection angle, that the effects of multiple scattering are unimportant here, despite the strong extinction (and the absence of detailed analysis); in any case, again, $\sigma_s \ll \sigma_e$ for the small particles.

3. EXPERIMENT

The argon ion laser beam first passed through a mechanical chopper to facilitate discrimination between the transmission signals and the plume radiation, and then divided into five components: one reference beam (≈10 percent) measured at the laser and four probe beams of approximately equal power directed through the plume. The laser, the chopper, and the beam-splitting and delivery optics were bolted to an aluminum bed integral to the trailer. A broadband radiometer was mounted on top of the transmitter housing to measure plume emission from a small region, roughly 10 cm in diameter, on the engine axis ≈76 cm from the exit plane; as discussed in the following section, these emission signals were used in background correction of the transmission data. The receiver was built on a 91×122×1.9 cm aluminum plate and employed four Burr-Brown® OPT210 silicon (Si) photodiode detectors, in which each detector was attached behind a 515-nm laser line filter to the output of a 10.2-cm integrating sphere. The integrating sphere was mounted at the focus of a 145-mm-diameter, 3.1 f-number (f/) glass lens and shielded by an infrared filter and a high-power dielectric attenuator. The attenuators (10:1) protected the integrating spheres from the laser irradiance, which was kept relatively high to compete well with the plume, and the bandpass filters were used, again, to assist in the separation of the laser and the plume signals. The instrument is sketched in figure 2 and a photo of the test stand and engine is given in figure 3.

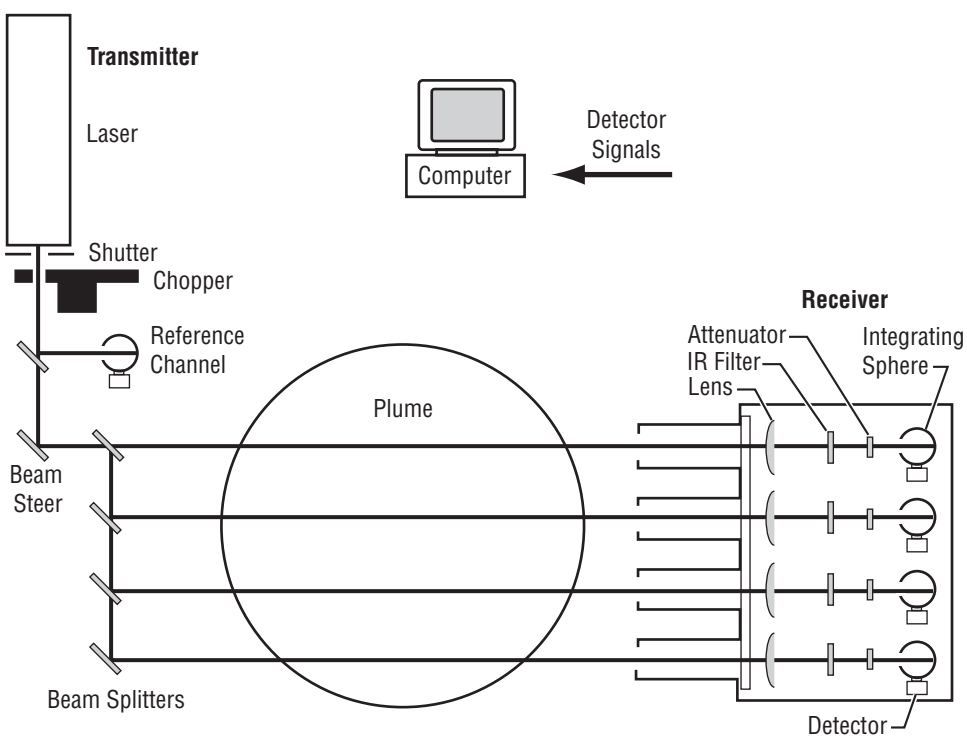

Figure 2. Schematic for the Fastrac transmissometer.

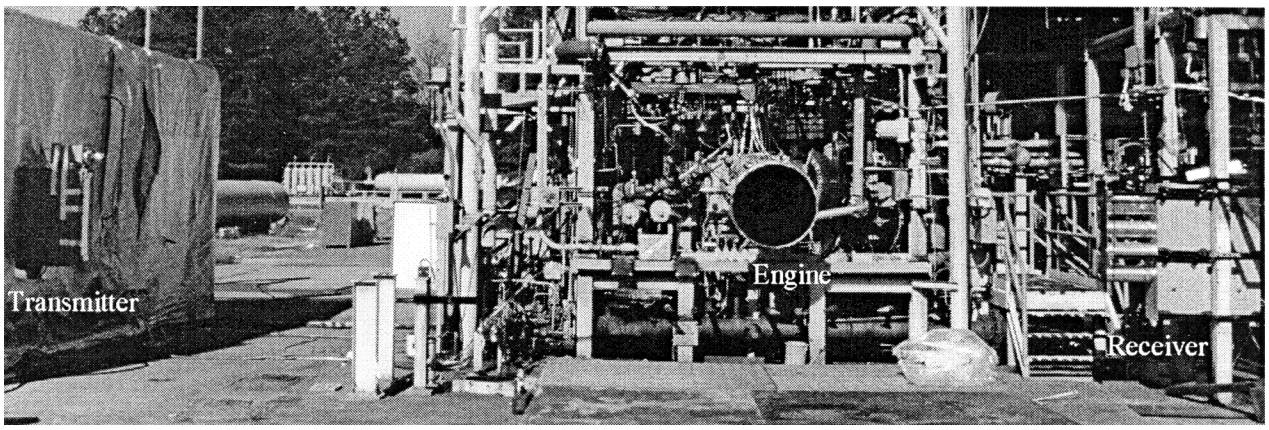

Figure 3. Photograph of Test Facility 116 Fastrac position showing the 60k-lb engine (right of center) and the laser tranmissometer (left and right flanks).

The lens and sphere combination provided a large target area for the laser beam, to accommodate some degree of alignment change during the firing. This design was in response to misalignment problems encountered in an earlier version of the instrument. The actual net laser spot travel at the lens location during an engine firing was measured for four tests in 1997 and found to be largely global in nature rather than characteristic of individual channels, suggesting that the main beam steering optic (and/or the laser cavity) was primarily responsible (see fig. 2). The average travel was ≈1.8 cm, with a maximum angular deflection of ≈0.35°. Although no studies of signal strength versus beam alignment were made in the field, measurements made in the laboratory before the instrument construction indicated that changes in signal strength for spot travel of this magnitude are typically <1 percent. In the final configuration, the acceptance angle of each receiver channel was limited by a 7.6-cm aperture mounted ≈76 cm in front of the collection optics; also, the receiver interior was shielded by a 1.27-cm-thick, heat-tempered glass window.

The signals from the receiver detectors were routed back to the trailer and measured using a MetraByte analog-to-digital converter (ADC) board inside a personal computer. The data sample rate was 20 kHz per channel, the voltage resolution was 12-bit, and the chopper frequency was ≈370 Hz. The data were stored initially in dynamic memory, sequentially alternating between separate buffers, and then the data in each buffer was written to the hard disk during the interval in which the alternate buffer was filling from the ADC. In this way the detector data were stored "real time" in static memory without interrupting the acquisition; the time between disk-writes was nominally 102.4 msec. Originally, problems were encountered with intermittent disk-write failures due to vibrations during the engine firing, but such failures could largely be avoided by using an older 244-megabyte hard drive rather than the newer 2.5-gigabyte hard drive (with a larger sector size). As a precaution, time stamps were written with the detector data, so that any gaps in the data would be obvious. In practice, gaps were brief and infrequent, typically only a few clock ticks (≈55 msec/tick) per gap occurring a few times during a firing lasting many tens of seconds.

The transmissometer was originally installed at the test stand to accommodate a somewhat different engine configuration and, as a result, the exact positioning of the laser beams within the plume of the 60k-lb engine was partially fortuitous. The beam locations are shown in figure 4. Because the engine axis was tilted ≈6° to the horizontal and the laser beams were in a vertical plane, there was a small axial variation in the beam placement (≈6.4-cm axial spread between the top and bottom beams). For reference, the nozzle diameter was ≈87 cm.

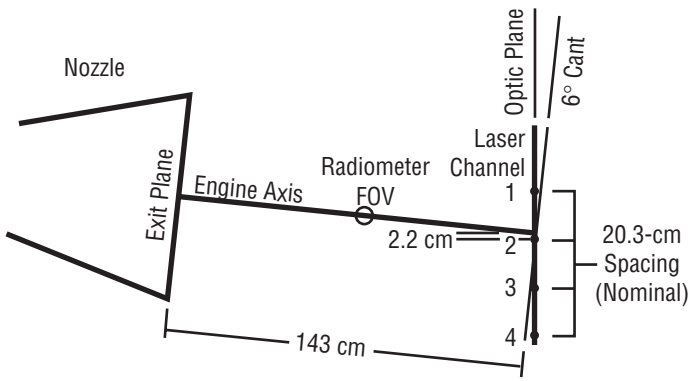

Figure 4. Fastrac engine transmissometer beam locations. The four horizontal laser beams, channels 1–4, are perpendicular to the engine axis and lie in a vertical plane ≈1.65 nozzle diameters from the exit plane. The engine axis is tilted ≈6° to the horizontal. Also shown is the position of the FOV for the radiometer used to monitor plume emission.

The argon laser control unit measures the output power of the laser, and this power was typically recorded before and following the engine firing; the unit itself was calibrated using a Spectra Physics model 405 power meter. This power level can be used with the reference channel data, which measures the relative output power, to determine the absolute output of the laser during the firing. The absolute output, in turn, can be used to calculate, from the reflective and transmissive properties of the delivery and collection optics, the laser power incident within the integrating spheres:

$$P \cong 0.0144\, T P_0 \quad , \tag{5}$$

where P_0 is the total output of the laser, P is the laser power entering one of the spheres (the nominal spread among the spheres is ≈1 percent), and the numerical coefficient is based on manufacturers' specifications. The accuracy of equation (5) is expected to be set by the reflectivity specification on the (high-power) beam splitters in the transmitter and is probably ≈15 percent, on average. The power, P, is of interest in estimating the plume radiance and in quantifying the ratio of laser to plume signals.

4. DATA ANALYSIS

The measurement of the chopper-modulated laser signals was performed separately from the data acquisition by subsequent analysis of the time-domain data. For the data taken before engine ignition and after shutdown, the chopper-open signals were simply corrected by subtracting adjacent chopper-closed signals, but during the firing, plume radiation contributed substantially to the detector signals generally, and background correction was based on plume-emission measurements. When the plume is present, half of the data on each transmission channel, taken during the blanking period of the chopper, consists only of plume radiation signals (and a small dark count), and it was found that these signals all resembled one another and the (unchopped) radiometer signal. Each of the laser channel plume signals was fitted, several seconds at a time, to the radiometer data by use of appropriate time shifts and voltage shifts, and the resulting time shifts were consistently characteristic of the spatial location on the plume of the detector field of view (FOV). The radiometer data, then, recorded during the chopper-open periods and time shifted and voltage shifted based on the chopper-closed data from both the radiometer and the laser channels, was used to background correct the laser transmission signals. This procedure was chosen chiefly because of the internal temporal consistency, but it also resulted in less erratic corrected signals than those based on interpolation by both least-squares polynomials and cubic spline fitting. The correlation among the emission signals from different locations in the plume was apparently a result of oscillations which were observed routinely in the chamber pressure data; the connection between the frequency spectra of plume emissions and chamber pressure has been noted previously, for example, in hybrid motors.[10]

The background-corrected signals were then averaged over individual chopper cycles and, since the laser power was variable during the tests, each channel was normalized to the reference channel, one chopper cycle at a time, calculating an rms scatter for the ratio during a cycle. This rms scatter was then used to inversely weight individual cycles in performing averaging over cycles; in this way, cycles for which the ratio of the transmission channel to the reference channel remains steady are favored in the averaging. For the results presented here, the final averages were over 360 cycles so that the time resolution is ≈1 Hz.

To determine plume transmissions from the normalized signals, it is necessary to calibrate the signals from beams transiting the plume by comparison with signals measured in the plume's absence (this too is a normalization, but is characterized here as a calibration to distinguish it from the reference channel normalization). The nominal procedure is to collect data both before and following the firing, and to use comparison between the pretest and posttest calibrations to quantify, in part, the uncertainty in the test data. In particular, the calibration error is defined as

$$\delta S_k = \frac{S_k - S'_k}{\frac{1}{2}(S_k + S'_k)} \quad , \tag{6}$$

where S_k and S'_k are the (normalized) pretest and posttest signals, respectively, for the kth laser channel (k=1–4). One practical consideration here is that cryogenic-generated water fog and posttest engine smoke

are important, but intermittent, sources of beam extinction in the test stand environment which must be avoided in calibrating the instrument.

The transmissions are interpreted in terms of axially symmetric models of the plume structure. The plume cross section is divided into concentric radial zones and the extinction coefficient is considered to be constant within each zone. Normally there is one zone for each beam so that the square (triangular) matrix problem (from eq. (1))

$$\ln(1 / T_k) = \sum_{j=1}^{k} L_{kj} \alpha_j \quad , \tag{7}$$

has a unique solution:

$$\alpha_j = \alpha_j(T_k, L_{kj}) \quad , \tag{8}$$

where T_k is the transmission of the kth beam, α_j is the extinction coefficient in the jth zone, and L_{kj} is the path length through zone j of beam k. The zone boundaries, especially the outermost case, are necessarily somewhat arbitrary and are defined here such that each boundary (along a line through the engine axis normal to and intersecting the beams) is centered between adjacent beams. The outer boundary is chosen simply to center the outer beam within the zone. The radial zones are shown in figure 5.

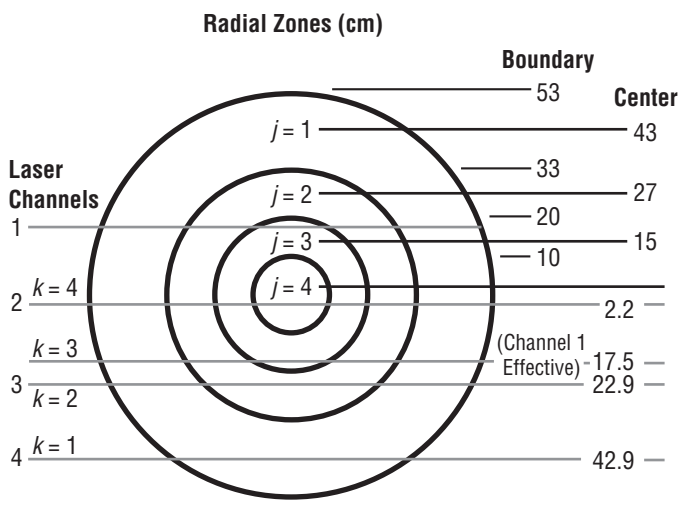

Figure 5. Radial zones defined for laser transmission through the Fastrac engine plume. The measured radial positions of the laser beams, shown on the lower right in centimeters, are used to define radial zones such that zone boundaries are equidistant from flanking beams. The resulting radial zone boundaries and centers are shown on the upper right, also in centimeters. The laser beams, depicted as gray lines with index k=1–4, are shown on the lower half of the plume,but note that the first beam (channel 1) is actually located above the centerline (see fig. 4).

For the extinction coefficient measurements, a mean transmission, T_k, and an rms deviation, Δ_k, about that mean are calculated for each of the four laser channels from a segment of data taken during the mainstage of the engine firing. The T_k are then used to generate a single set of coefficients, α_j, for each firing. The error bars, $\Delta\alpha_j$, for the coefficient measurement are estimated by direct calculation of the rms scatter about $\alpha_j(T_k,L_{kj})$ of the coefficients $\alpha_{j,n}(T_{k,n},L_{kj})$, evaluated for the transmissions

$$T_{k,n} = T_k\left[\left(1+\delta S_k\right)\left(1+\frac{\Delta_k}{T_k}\right)\right]^{m_k} \quad , \quad m_k = -1,0,1; \quad n = 1-P \quad , \tag{9}$$

where the index n represents a unique combination of the indices m_k, k=1–4, and $P = 3^4$ is the total number of such combinations. This approach, although simplistic in its use of equation (9), permits initial averaging over T_k (which is directly measured) in preference to α_j (which is derived), and combines the two error sources, δS_k and Δ_k, in a single operation. Note that the sequence k = 1–4, from the outside in, is, from figure 5, laser channel = 4, 3, 1, 2.

Because the instrument was limited to four beams, the resolution of the plume into radial zones was fairly coarse. It is expected that the distribution of extinction coefficients within the plume would be more realistically modeled with additional zones. For this reason, solutions were also calculated for an eight-zone model defined by dividing into two each of the zones of figure 5. These solutions, which are underdetermined and thus nonunique, were calculated by fitting the plume transmissions to coefficient distributions using a function minimization routine. In particular, Powell's direction set method was used to vary the coefficients α_j in minimization of the merit function

$$\mu = \sqrt{\frac{1}{N}\sum_{k=1}^{N}\left\{\left[\left(\sum_{j=1}^{M}\alpha_j L_{kj}\right) - \ln\left(\frac{1}{T_k}\right)\right]\left(\sum_{j=1}^{M} L_{kj}\right)^{-1}\right\}^2} \quad , \tag{10}$$

where N is the number of beams (4) and M is the number of zones (L_{kj}= 0 effectively limits the j sums). For efficiency, the root extraction and the total path normalization were omitted in the fitting iterations, but the merit function in the form given in equation (10) is used here to quantify the fit quality in terms of dimensions and magnitudes appropriate to the solution α_j. For the eight-zone model, the solutions given here are as examples of physical distributions which are consistent with the present measurements.

As discussed in the next section, equation (10) is also useful as an alternative in the four-zone model, for which the solutions are both unique and, by design, nonnegative. In this case, the coefficient is calculated as a merit function weighted average, and the error bars are, in consequence, likewise weighted averages:

$$\overline{\alpha}_j = \left(\sum_{n=1}^{P}\mu_n^{-1}\right)^{-1}\sum_{n=1}^{P}\mu_n^{-1}\alpha_{j,n}, \quad \Delta\alpha'_j = \sqrt{\left(\sum_{n=1}^{P}\mu_n^{-1}\right)^{-1}\sum_{n=1}^{P}\left[\mu_n^{-1}(\alpha_{j,n}-\overline{\alpha}_j)^2\right]} \quad , \tag{11}$$

where $\alpha\varphi$, v and μ_n are the coefficient and merit function, respectively, for the nth permutation in equation (9). In this way, the results are biased in favor of solutions that are internally consistent.

5. RESULTS AND CONCLUSIONS

The data presented here are from five firings: two short-duration and three long-duration tests, from February through July 1998. The firing conditions for the tests were, except for duration, very similar; the chamber pressure varied by ≈3 percent and the nozzles were approximately identical. It is notable, however, that for the last two tests (23 and 24), two jet vanes were installed 90° apart at the exit plane near the edge of the nozzle for purposes of materials testing.

For the two short-duration firings, each ≈20 sec, agreement between pretest and posttest calibrations ranged from approximately 2 to 15 percent, as shown in table 1 (there was a mechanical failure of the channel 4 detector assembly shortly after engine ignition on test 21). The average agreement for the data shown is 7 percent, and, because of the dearth of individual channel data, this value is used for δS_k of equation (6); i.e., $\delta S_k = \delta S \equiv 0.07$, all k. The reason for the poor agreement in the lower channels (3 and 4) is not known, but two possible sources of error are posttest fog and/or smoke-obscuration, and detector heating. Typical times for general clearing of the area following engine shutdown were many tens of seconds, and posttest data acquisition was limited by larger considerations to a variable period not exceeding a few minutes. However, obscuration tends to be intermittent in nature, and the data suggest a pervasive effect. It is also possible that the internal temperature of the receiver housing continued to rise in this period and, as discussed below, detector heating was a substantial problem on the long-duration tests. It is also worth mention here that obscuration during the firing, which would obviously and directly corrupt the transmission results, was, while not systematically eliminated as a possibility, generally not observed. An example of the short test data is given in figure 6, which shows the transmission results for test 20.

Table 1. Averages of pretest and posttest calibration signals, normalized to the reference channel, and the fractional difference δS_k (eq. (6)) between those averages for the two short-duration tests.

	Channel							
	1		2		3		4	
Test	Mean	δS_k	Mean	δS_k	Mean	δS_k	Mean	δS_k
20	0.696	0.0688	0.723	0.0638	0.752	0.0418	0.275	0.151
21	0.675	0.0168	0.709	–0.0151	0.670	0.138	–	–

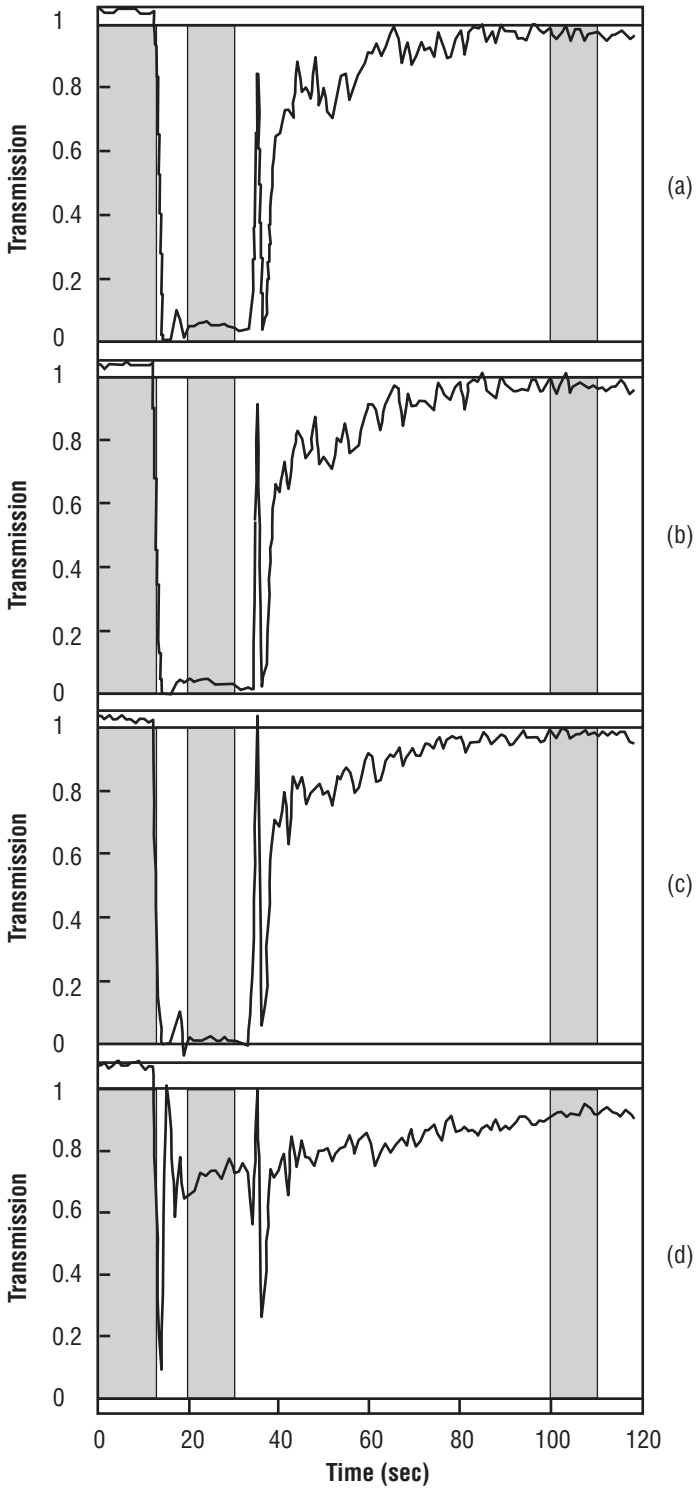

Figure 6. Transmission data for short-duration test: test 20. Figure 6(a)–(d) give channels 1–4 normalized to the reference channel and calibrated from the average of signals in pretest and posttest calibration windows, shown as gray regions. Mainstage transmission is also shown in gray.

During the long-duration firings, each ≈2.5 min, plume heating of the receiver (see fig. 3) resulted in degradation of the detector signals, apparently due to substantial heating of the electronic circuits, so that only the data early in the firing are useful, and posttest calibration was not feasible. An example of a transmission curves for a long-duration test is given in figure 7. Based on the time behavior of the signals during the long-duration tests, and on the results of the short-duration tests, the assumption was made that the first 30 sec of mainstage data should reliably reflect the plume transmission. Data from later in the long-duration firings, including the posttest data, were not used for the results.

Table 2 gives the mainstage transmissions T_k and the rms Δ_k (subscripts omitted) for the five tests for the four spatial channels. Again, the transmissions for the long-duration tests are calibrated using pretest data only.

Table 2. Average transmissions T_k and their rms deviations Δ_k for the 60k-lb Fastrac engine.

	Channel							
	1		2		3		4	
Test	T	Δ	T	Δ	T	Δ	T	Δ
19	0.0527	0.0064	0.0427	0.0116	0.0193	0.0060	0.4954	0.0460
20	0.0549	0.0052	0.0375	0.0076	0.0150	0.0047	0.7205	0.0294
21	0.0491	0.0087	0.0262	0.0081	0.0119	0.0070	–	–
23	0.0405	0.0069	0.0522	0.0141	0.0196	0.0106	0.6736	0.0353
24	0.0299	0.0067	0.0900	0.0234	0.0225	0.0094	0.6133	0.0135

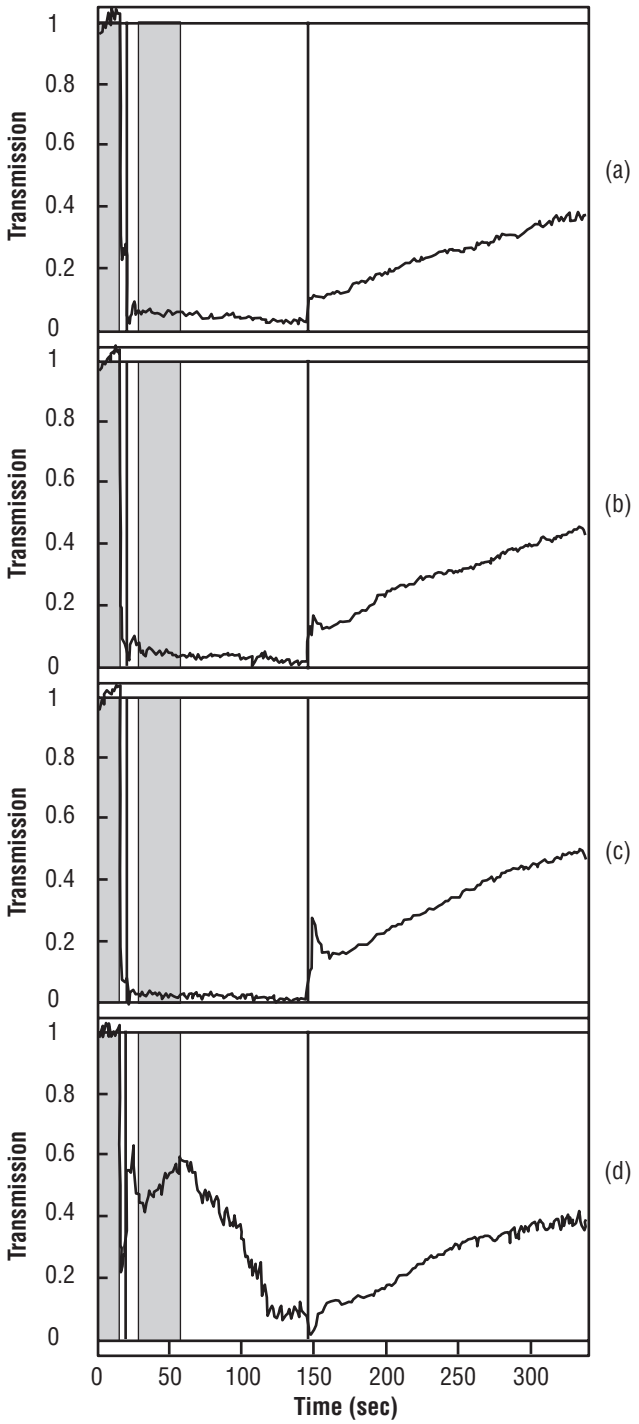

Figure 7. Transmission data for a long-duration test: test 19. Figure 7(a)–(d) give channels 1–4 normalized to the reference channel and calibrated from the pretest calibration window, shown as a gray region. Mainstage transmission is also shown grayed, and engine startup and shutdown are shown as vertical lines. The decline in signal after ≈70 sec is due to heating of the detectors and not to decreasing transmission.

Table 3 gives algebraic solutions α_j of equation (7) for the T_k of table 2 in the four-zone model along with error bars calculated from the $T_{k,n}$ in equation (9). Also shown is the mean mass density of carbon soot in the Rayleigh limit, including an estimated error bar calculated analogously to $\Delta\alpha_j$. The largest extinction is consistently in the $j = 2$ zone, with its center radius of 27 cm, but, notably excepting test 24, the center zone also shows distinct opacity (tests 23 and 24 nominally show a somewhat more uniform distribution interior to $j = 2$ than do tests 19 and 20). The spatially averaged mass density for the plume is very similar for all the tests. The negative extinction coefficients in the table are physically unreal and are due to the errors in the transmission measurements.

Table 3. Extinction coefficients α_j from equation (7) and the T_k, and error bars $\Delta\alpha_j$ from equation (7) and the $T_{k,n}$ from equation (9), both in m^{-1}, for radial zones of the Fastrac engine plume for the four-zone model (algebraic solution). The right column is the mass density of Rayleigh soot and the error bar for η_0 is calculated analogously to $\Delta\alpha_j$.

Test	Zone j (Center Channel)				$\bar{\eta}_0 \left(\frac{\mu g}{cm^3}\right)$
	1(4)	2 (3)	3 (1)	4 (2)	
19	1.140 ± 0.207	7.24 ± 0.625	−0.580 ± 1.28	5.16 ± 1.59	0.665 ± 0.0270
20	0.532 ± 0.143	8.40 ± 0.610	−1.50 ± 1.230	6.57 ± 1.34	0.627 ± 0.0220
23	0.642 ± 0.157	7.72 ± 0.883	0.985 ± 1.78	2.80 ± 1.73	0.639 ± 0.0288
24	0.794 ± 0.119	7.26 ± 0.734	2.96 ± 1.68	−1.92 ± 1.80	0.650 ± 0.0286

One feature of the measured transmissions is that, although the difference is not striking, the channel 3 transmissions are consistently smaller than those of the effectively nearby channel 1 (see table 2). The effective radial (axial) separation of these beams is in fact only about 1/16 (1/20) of a nozzle diameter, and the transmission differential, interpreted at face value, would thus imply a steep spatial gradient in the soot distribution in this region (it is also possible, of course, to interpret the differential as due to axial asymmetry). In light of the significant errors in the measurements and the close spacing, it is worth comparing the nominal results of table 3 with a two-zone interpretation, in which the inner three zones of figure 5 are combined and the transmissions and path lengths for the three beams are averaged. The inner zone extinction coefficients and mean soot densities for this two-zone calculation are given in table 4; the outer zone coefficients are, of course, the same as in table 3.

Table 4. Center zone extinction coefficients and mean soot densities for the two-zone model. The outer zone (j=1) coefficients are the same as in table 3.

Test	$\Delta\alpha_{center}$ (m^{-1})	$\bar{\eta}_0 \left(\frac{\mu g}{cm^3}\right)$
19	4.95	0.680
20	5.54	0.643
23	5.37	0.643
24	4.83	0.613

As an additional check, the transmissions for channels 1 and 3 (table 2) were averaged together, effectively combining the j = 2 and 3 zones (and shifting the beams slightly so that channel 2 was on the engine axis). This three-zone interpretation produces coefficients (not explicitly given) in the center zone comparable to those of the outer zone (essentially j = 1 of table 3) and in the intermediate zone comparable to those of the j = 2 zone of table 3, so that the distribution is again annular (the mean mass densities are also similar).

The extinction coefficient distribution can also be calculated in the four-zone model by use of the merit function (eq. (10)) solution of equation (7). In this case, the α_j are chosen on the basis of the best fit to the data T_k (and L_{kj}) and the merit function quantifies the accuracy of the fit. Table 5 gives the fitting solutions for the four-zone model and table 6 gives the results of the weighted average and error bar calculations from equation (11).

Table 5. Extinction coefficients α_j, in m^{-1}, from the fitting using equation (10) for radial zones of the Fastrac engine plume for the four-zone, best-fit model (no α<0). Shown on the right are the merit function μ for the fit, also in m^{-1}, and the mean mass density of Rayleigh soot.

Test	Zone j (Center Channel)				μ(m^{-1})	$\bar{\eta}_0 \left(\frac{\mu g}{cm^3}\right)$
	1(4)	2 (3)	3 (1)	4 (2)		
19	1.130	7.14	6.08E–16	4.69	0.0478	0.669
20	0.493	8.14	1.30E–17	5.37	0.123	0.637
23	0.642	7.72	0.985	2.80	2.19E–15	0.639
24	0.768	7.38	1.93	2.36E–17	0.123	0.640

Table 6. Average extinction coefficients $\overline{\alpha}_j$ and error bars $\Delta\alpha'_j$ from equation (11), in m^{-1}, for radial zones of the Fastrac engine plume for the four-zone, best-fit model (no α<0). Shown on the right are the average merit functions, $\overline{\mu}$, for the fits, also in m^{-1}, and the mean mass density of Rayleigh soot.

Test	Zone *j* (Center Channel)				$\overline{\mu}(m^{-1})$	$\overline{\eta}_0 \left(\frac{\mu g}{cm^3}\right)$
	1(4)	2 (3)	3 (1)	4 (2)		
19	1.13 ± 0.148	6.92 ± 0.217	0.468 ± 0.497	5.45 ± 0.671	0.0717	0.707 ± 0.0218
20	0.683 ± 0.0873	7.52 ± 0.0890	0.508 ± 0.0343	5.23 ± 0.0299	0.129	0.642 ± 0.00712
23	0.647 ± 0.139	6.82 ± 0.430	2.86 ± 1.19	2.31 ± 1.66	0.0295	0.634 ± 0.0258
24	0.681 ± 0.0824	7.46 ± 0.847	2.15 ± 1.01	0.478 ± 0.361	0.133	0.642 ± 0.0300

For comparison, several arbitrary solutions for the coefficient distributions using equation (10) in the eight-zone model are plotted in figures 8–11, along with graphs of the table 5 distributions. The latitude afforded by the additional zones results in machine zero merit functions for these fits. The only constraint is that solutions with large peripheral extinctions were discouraged because of the uncertainty in the outer zone boundary and because of the sensitivity of the spatial mean to the periphery extinction (area goes like the square of the radius). The resulting mean soot densities are very similar to those of the several four-zone solutions.

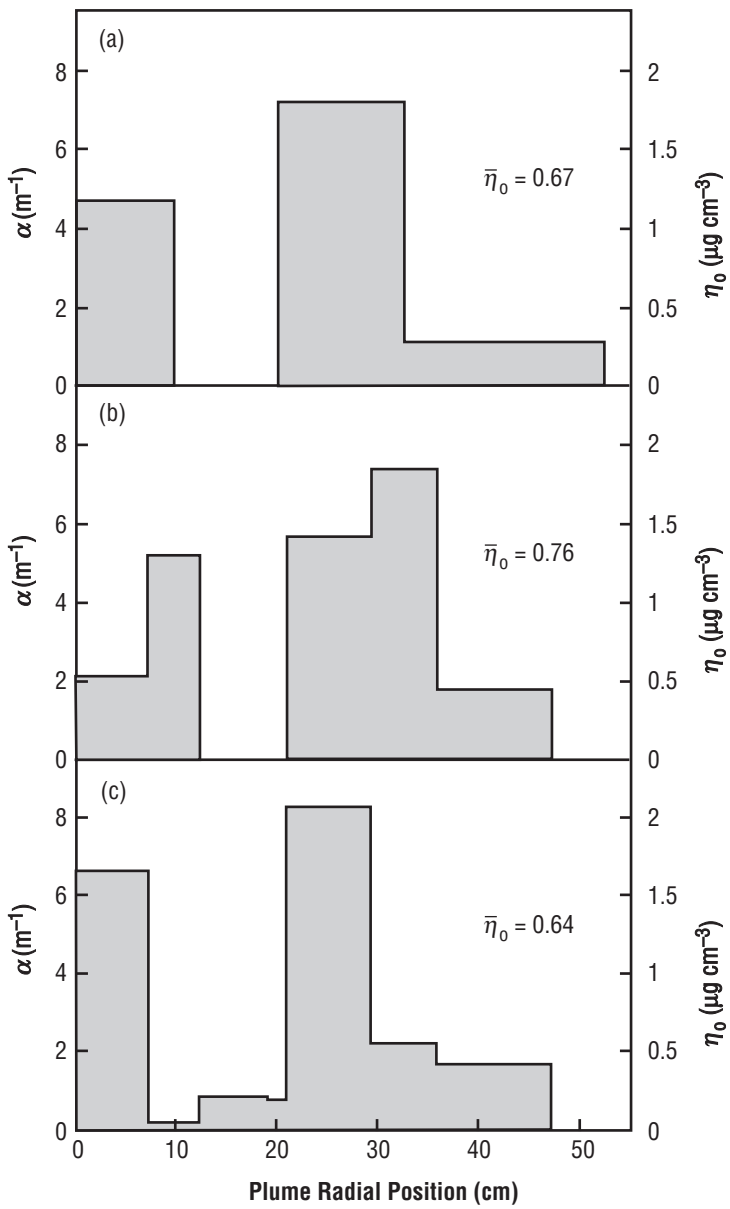

Figure 8. Extinction coefficient/soot density distributions for test 19. The coefficient (left) and the density (right) are plotted as functions of the radial position in the plume, where zero is the axis. (a) four-beam/four-zone solution (b) and (c) two (underdetermined) solutions in an eight-zone model. The density values are for carbon soot in the Rayleigh limit.

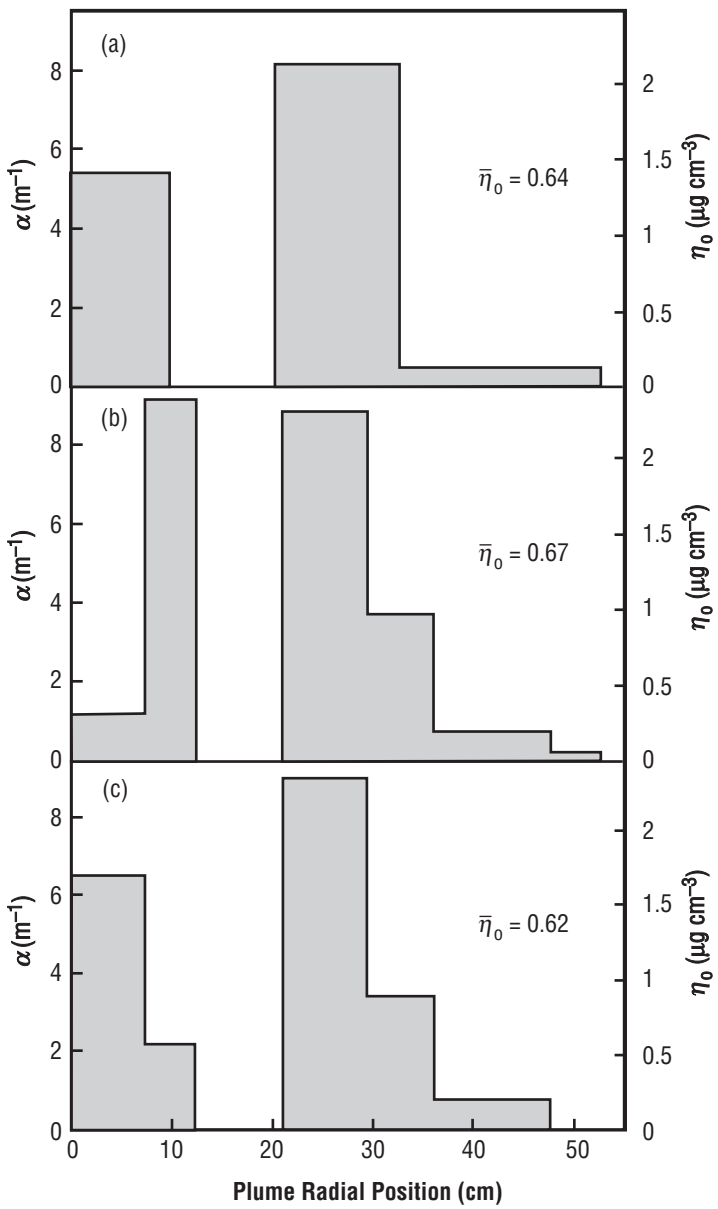

Figure 9. Extinction coefficient/soot density distributions for test 20. The coefficient (left) and the density (right) are plotted as functions of the radial position in the plume, where zero is the axis. (a) four-beam/four-zone solution (b) and (c) two (underdetermined) solutions in an eight-zone model. The density values are for carbon soot in the Rayleigh limit.

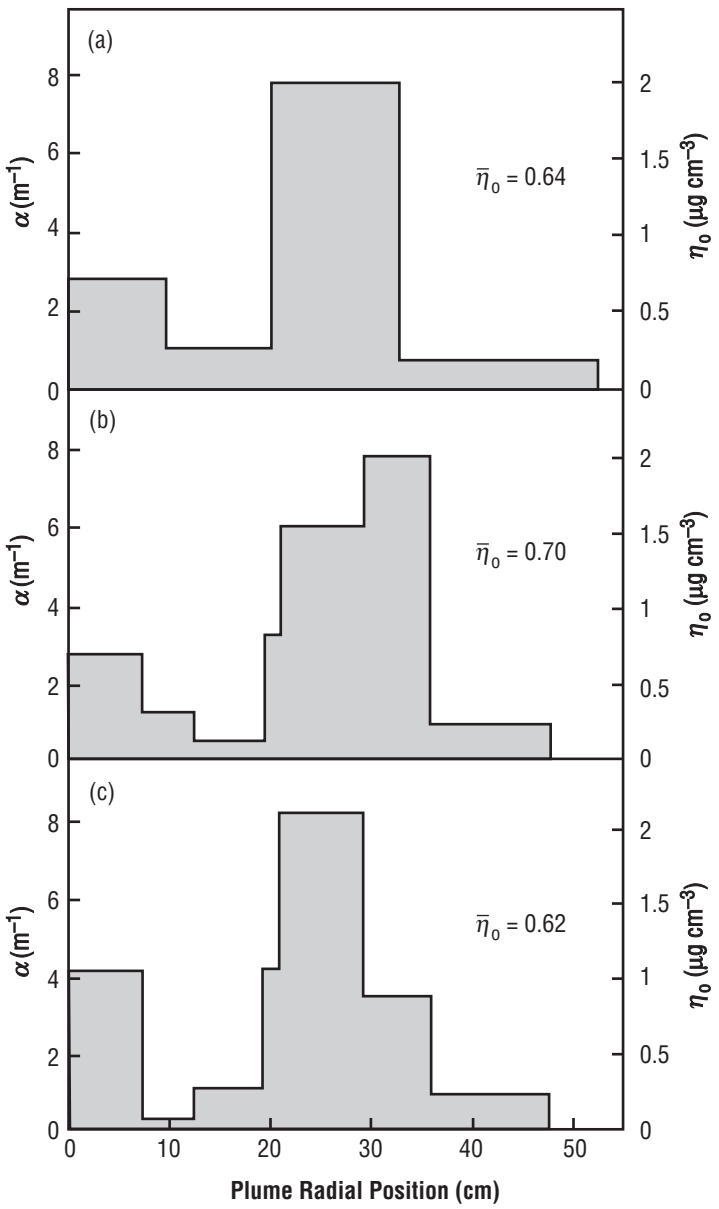

Figure 10. Extinction coefficient/soot density distributions for test 23. The coefficient (left) and the density (right) are plotted as functions of the radial position in the plume, where zero is the axis. (a) four-beam/four-zone solution (b) and (c) two (underdetermined) solutions in an eight-zone model. The density values are for carbon soot in the Rayleigh limit.

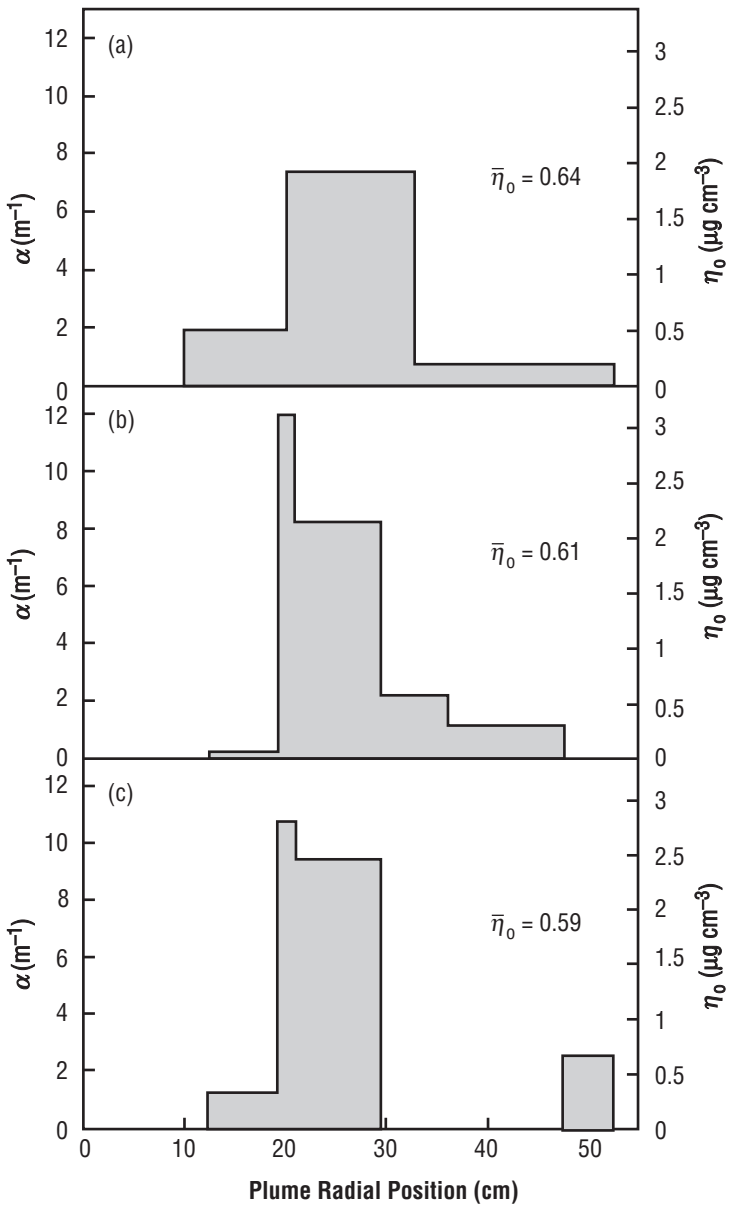

Figure 11. Extinction coefficient/soot density distributions for test 24. The coefficient (left) and the density (right) are plotted as functions of the radial position in the plume, where zero is the engine axis. (a) four-beam/four-zone solution (b) and (c) two (underdetermined) solutions in an eight-zone model. The density values are for carbon soot in the Rayleigh limit.

Although the plume emission was of primary interest in the transmissometry as a background correction, there is both intensity and frequency information on the plume emission, in its own right, available as a result of the data analysis. As indicated above, the plume radiance can be estimated from knowledge of the actual laser power at the detectors. As a specific example, the top two channels for test 21, which are noteworthy in the agreement between pretest and posttest calbrations, show measured average signals before the firing of 3.64 and 3.77 V, respectively, which, from equation

(5) with P_0 = 1,220 mW and T=1, give 0.207 and 0.215 V/mW, respectively. The average plume signals on these channels during the firing, based on chopper-closed data during (and before) the firing, are 0.515 and 0.683 V, corresponding to 2.49 and 3.18 mW, respectively. From ray-trace calculations, the FOV of the sphere aperture on the plume is circular with FWHM values, at the engine axis, of 14 and 19 cm, respectively, for the two spheres (channel 1 has a 2.5-cm-diameter aperture and channels 2–4 have 3.3-cm-diameter apertures); and the acceptance solid angle of the receiver is set by the barrel apertures (see fig. 2) to 6.7×10^{-4} sr (f/34). Also, the acceptance cone of the Si chip in the detectors is set by the geometry of the assembly to ≈13°, half-angle, so that the nominal 10-nm FWHM of the interference filter (515.4 nm) atop the chip becomes ≈20 nm.[11] Thus the plume radiance, again, using the axial FOV as an effective surface area, comes to approximately 1.2 and 0.84 $Wcm^{-2}sr^{-1}\mu m^{-1}$, respectively, for the two channels. For reference, these radiances correspond to blackbody temperatures of ≈2,200 K.

From equation (5) and the test 21 reference channel data ($P_{0,mainstage} \cong 0.62\ P_{0,pretest}$) and measured transmissions (see table 2), the average laser power entering the channel 1 and 2 spheres during the firing would be approximately 0.535 and 0.285 mW, respectively, or about 0.21 and 0.09 of the respective plume signals, which indicates directly the magnitude of the discrimination problem. In this connection, it is worth noting that an order of magnitude improvement over the laser signals obtained with the instrument used here would be straightforward technologically, given commercially available lasers. Also of note is that the 13° acceptance half-angle of the detectors, along with the 2.8-cm recession of the Si chip, results in ≈10 percent of the interior surface of each sphere being sampled by its detector.

Table 7 gives the time shifts determined from correlation of the plume emission signals in background-correcting the transmission data. The absolute values of the shifts are relevant only in that the radiometer data originate from an axial position in the plume that is ≈67 cm upstream of the optic plane of the transmissometer (see fig. 4). Note that all the mainstage data are used in the averages given in table 7 since the frequency response of the detectors was apparently unaffected by the heating.

Table 7. Time shifts and rms deviations, in μsec, for correlation between emission signals from the laser channels and emission signals from the radiometer; the FOV of the radiometer is on the engine axis ≈76 cm from the exit plane. Numbers in parentheses are deviations in percentage.

Test	Channel			
	1	2	3	4
19	570 ± 72.2 (12.7)	270 ± 73.3 (27.2)	606 ± 50.2 (8.27)	637 ± 113 (17.7)
20	519 ± 25.9 (4.99)	343 ± 38.8 (11.3)	552 ± 24. (4.35)	588 ± 30.3 (5.15)
21	505 ± 32.8 (6.48)	345 ± 18.5 (5.37)	544 ± 22.2 (4.08)	–
23	502 ± 47.7 (9.5)	267 ± 53.1 (19.9)	598 ± 54.6 (9.14)	517 ± 45.7 (8.83)
24	505 ± 52.8 (10.5)	278 ± 40.7 (14.6)	617 ± 42.8 (6.94)	500 ± 64.5 (12.9)

To summarize, the observed transmissions of the argon ion laser beams through the Fastrac engine plume may be straightforwardly interpreted as due to a generally central and evidently annular soot distribution, with the highest densities near the 25-cm radial position and at the center. Some latitude in this interpretation is possible and the primary uncertainties are in particle size and shape and from the measurement error bars. For soot particle diameters less than ≈20 nm, the spatially averaged soot mass density implied by the data is ≈0.7 $\mu g\ cm^{-3}$. For aspherical particles, or for intermediate-sized spherical particles (≈50 to 300 nm diameters), the implied mass density is generally somewhat smaller, and for really large particles (supermicron diameters) the densities are expected to be distinctly larger.

REFERENCES

1. Farmer, R.C.; and Anderson, P.G.: "Soot Formation in Rocket Propulsion Systems," *Final Report,* Contract No. SECA–FR–95–12, June 1995.

2. Jennings, S.G.; and Pinnick, R.G.: "Relationships Between Visible Extinction, Absorption and Mass Concentration of Carbonaceous Smoke," *Atmospheric Environment*, Vol. 14, pp. 1123–1129, 1980.

3. Bernard, J.M.: "Particle Sizing in Combustion Systems Using Scattered Laser Light," *Report No. TR–0086A (2060)–3 (SD–TR–88–37)*, May 1988.

4. Lyons, V.J.: "Optical Measurements of Soot in Premixed Flames," *Ph.D. Thesis*, California University, Berkeley, CA, August 1988.

5. Charalampopoulos, T.T.; and Felske, J.D.: "Refractive Indices of Soot Particles Deduced From In Situ Laser Light Scattering Measurements," *Combustion and Flame*, Vol. 68, pp. 283–294, 1987.

6. Pike, J.: "FAS Space Policy Project World Space Guide," URL: http://www.fas.org/spp/guide/usa/launch/x-34.htm (cited March 13, 1999).

7. Coulson, K.L.: "Scattering of Light by Nonspherical Particles," *Report No. UCID–20609 (DE86 004666)*, Lawrence Livermore National Laboratory, Livermore, CA, December, 1985.

8. Dobson, C.C.; and Lewis, J.W.L.: "Survey of the Mie Problem Source Function," *Journal of the Optical Society of America*, Vol. 6, No. 3, pp. 463–466, March 1989.

9. Weast, R.C.; Astle, M.J.; and Beyer, W.H. (eds.): *CRC Handbook of Physics and Chemistry,* 64th ed.; CRC Press, Inc., Boca Raton, FL, 1984.

10. Lee, M.H.; et al.: "Pressure Oscillations in a Laboratory Scale Hybrid Motor," *NASA Conference Publication 3283*, Vol. II, p. 162, September 1994.

11. Corion Corporation, *Optical Filters and Coatings*, Corion catalog, Holliston, MA, May 1990.

REPORT DOCUMENTATION PAGE

Form Approved
OMB No. 0704-0188

Public reporting burden for this collection of information is estimated to average 1 hour per response, including the time for reviewing instructions, searching existing data sources, gathering and maintaining the data needed, and completing and reviewing the collection of information. Send comments regarding this burden estimate or any other aspect of this collection of information, including suggestions for reducing this burden, to Washington Headquarters Services, Directorate for Information Operation and Reports, 1215 Jefferson Davis Highway, Suite 1204, Arlington, VA 22202-4302, and to the Office of Management and Budget, Paperwork Reduction Project (0704-0188), Washington, DC 20503

1. AGENCY USE ONLY *(Leave Blank)*

2. REPORT DATE
March 2000

3. REPORT TYPE AND DATES COVERED
Technical Publication

4. TITLE AND SUBTITLE
Laser Transmission Measurements of Soot Extinction Coefficients in the Exhaust Plume of the X–34 60k-lb Thrust Fastrac Rocket Engine

5. FUNDING NUMBERS

6. AUTHORS
C.C. Dobson, R.H. Eskridge, and M.H. Lee

7. PERFORMING ORGANIZATION NAMES(S) AND ADDRESS(ES)
George C. Marshall Space Flight Center
Marshall Space Flight Center, AL 35812

8. PERFORMING ORGANIZATION REPORT NUMBER
M–972

9. SPONSORING/MONITORING AGENCY NAME(S) AND ADDRESS(ES)
National Aeronautics and Space Administration
Washington, DC 20546–0001

10. SPONSORING/MONITORING AGENCY REPORT NUMBER
NASA/TP—2000–210075

11. SUPPLEMENTARY NOTES
Prepared for Propulsion Research Center, Space Transportation Directorate

12a. DISTRIBUTION/AVAILABILITY STATEMENT
Unclassified-Unlimited
Subject Category 20
Standard Distribution

12b. DISTRIBUTION CODE

13. ABSTRACT *(Maximum 200 words)*
A four-channel laser transmissometer has been used to probe the soot content of the exhaust plume of the X–34 60k-lb thrust Fastrac rocket engine at NASA's Marshall Space Flight Center. The transmission measurements were made at an axial location ≈1.65 nozzle diameters from the exit plane and are interpreted in terms of homogeneous radial zones to yield extinction coefficients from 0.5–8.4 per meter. The corresponding soot mass density, spatially averaged over the plume cross section, is, for Rayleigh particles, ≈0.7 μg cm^{-3}, and alternative particle distributions are briefly considered. Absolute plume radiance at the laser wavelength (515 nm) is estimated from the data at ≈2,200 K equivalent blackbody temperature, and temporal correlations in emission from several spatial locations are noted.

14. SUBJECT TERMS
rocket engine, soot, laser, transmission, extinction

15. NUMBER OF PAGES
36

16. PRICE CODE
A03

17. SECURITY CLASSIFICATION OF REPORT
Unclassified

18. SECURITY CLASSIFICATION OF THIS PAGE
Unclassified

19. SECURITY CLASSIFICATION OF ABSTRACT
Unclassified

20. LIMITATION OF ABSTRACT
Unlimited